Slow-muon study of quaternary solar-cell materials: Single layers and *p-n* junctions

H. V. Alberto,[1,*] R. C. Vilão,[1] R. B. L. Vieira,[1] J. M. Gil,[1] A. Weidinger,[2] M. G. Sousa,[3] J. P. Teixeira,[3] A. F. da Cunha,[3] J. P. Leitão,[3] P. M. P. Salomé,[3,4] P. A. Fernandes,[3,4,5] T. Törndahl,[6] T. Prokscha,[7] A. Suter,[7] and Z. Salman[7]

[1]*CFisUC, Department of Physics, University of Coimbra, R. Larga, P-3004-516 Coimbra, Portugal*
[2]*Helmholtz-Zentrum Berlin für Materialien und Energie, D-14109 Berlin, Germany*
[3]*I3N and Department of Physics, University of Aveiro, Portugal*
[4]*International Iberian Nanotechnology Laboratory, P-4715-330 Braga, Portugal*
[5]*CIETI and Departament of Physics, Instituto Superior de Engenharia do Porto, P-4200-072 Porto, Portugal*
[6]*Ångström Laboratory, Solid State Electronics, Ångström Solar Center, Uppsala University, SE-75121 Uppsala, Sweden*
[7]*Laboratory for Muon Spin Spectroscopy, Paul Scherrer Institut, CH-5232 Villigen PSI, Switzerland*

(Received 19 September 2017; published 8 February 2018)

Thin films and *p-n* junctions for solar cells based on the absorber materials $Cu(In,Ga)Se_2$ and Cu_2ZnSnS_4 were investigated as a function of depth using implanted low energy muons. The most significant result is a clear decrease of the formation probability of the Mu^+ state at the heterojunction interface as well as at the surface of the $Cu(In,Ga)Se_2$ film. This reduction is attributed to a reduced bonding reaction of the muon in the absorber defect layer at its surface. In addition, the activation energies for the conversion from a muon in an atomiclike configuration to a anion-bound position are determined from temperature-dependence measurements. It is concluded that the muon probe provides a measurement of the effective surface defect layer width, both at the heterojunctions and at the films. The CIGS surface defect layer is crucial for solar-cell electrical performance and additional information can be used for further optimizations of the surface.

DOI: 10.1103/PhysRevMaterials.2.025402

I. INTRODUCTION

Thin film solar cells using $Cu(In,Ga)Se_2$ (CIGS) as the p-type absorber and CdS as the buffer layer, are a successful technology, with power conversion efficiencies already exceeding 22% [1]. The sparse availability of some of the materials (In, Ga) and possible environmental hazards related to the use of Se in the absorber and Cd in the buffer layer have prompted intensive research for alternative solutions. Cu_2ZnSnS_4 (CZTS) is structurally similar to CIGS and offers the advantage of being based only on earth-abundant elements. However, its performance in solar-cell devices is still poor compared to CIGS [2]. For the buffer layer, ZnSnO has been suggested as a promising Cd-free material [3]. In the present work, various combinations of absorber and window materials were investigated.

This work uses implanted positive muons, μ^+, as probes in these materials. Muon spin spectroscopy (μSR) is a well-established technique providing information on the role of isolated hydrogen in semiconductors [4,5], since the positive muon behaves as a light isotope of hydrogen. Implanted muons may thermalize as an unbound muon or may capture one or even two electrons inside the material, forming different muonium charge states (Mu^+, Mu^0, and Mu^-) similar to the corresponding hydrogen states (H^+, H^0, and H^-). We reserve the Greek letter μ^+ for the incident particle, in vacuum, whereas inside the material the positive state will be denoted by Mu^+, analogous to H^+. The μSR parameters associated with the different muonium charge states and configurations have also been shown to be sensitive to interactions with charge carriers [6–10] and to the presence of an external electric field. In addition, the formation probability of the different muonium states is known to be sensitive to the presence of defects [11–14].

In semiconductors, different configurations of the embedded muon can be distinguished [6,7] as follows:

(i) Atomlike muonium, denoted by Mu^0_{atom}, at an open interstitial site in the lattice; this state has a large hyperfine interaction in the order of GHz, close to the vacuum value [6,7].

(ii) A bound configuration where the muon is incorporated in the bonding structure of the lattice. In this configuration, the muon may exist as positive state (Mu^+) or as muonium (Mu^0_{bound}). This latter state is paramagnetic but its hyperfine interaction is orders of magnitude smaller than the vacuum value, and may be barely distinguishable from the diamagnetic state [15,16].

(iii) Negative muonium, Mu^-; this state is predicted in theoretical calculations [15,17–20] but its formation probability is small compared with other charged states since the formation of Mu^- is a two-stepped process requiring the capture of two electrons in the implantation, an unlikely event.

The study of thin films using implanted positive muons is possible only in the Low Energy Muon facility (LEM) [9,21], at the Paul Scherrer Institut (PSI), Switzerland. In LEM the muons are first moderated to almost thermal energies and subsequently accelerated in an electrostatic field. In this way depth profiles with a depth resolution in the order of tens of nanometers, depending on material and distance from the surface, can be achieved. Semiconductor films (Si, Ge) have been investigated using low energy muons and the observed changes of the μSR parameters (fractions and relaxations)

*lena@fis.uc.pt

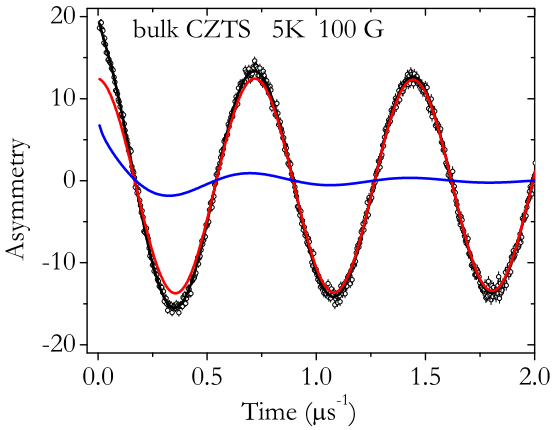

FIG. 1. μSR time spectrum of bulk CZTS at $T = 5$ K, in transverse geometry ($B = 10$ mT). The red line is the main component of the signal, fitted with a Gaussian-damped cosine and is assigned to muons at an anion-bound configuration. The blue line is a fast-relaxing component with a depolarization rate $\lambda = 8(1)\,\mu s^{-1}$, related to muons at an interstitial position. The black line is the sum of the two components.

as a function of depth in the sample were correlated with charge carrier effects [8–10,22], in particular with a carrier depletion zone in the near-surface region [14]. The formation of muonium states in CZTS was also investigated, both in bulk and thin films [13]. It was found that the majority of the muons are bound to sulfur, most likely in a Mu^+ charged state (see Fig. 1). At low temperatures (below around 150 K), however, a fraction between 20% and 40% of the muons may also form a neutral state in an interstitial position. First-principle calculations in Cu(In,Ga)Se_2 [23,24] found that H^+ takes up an equilibrium position at the Cu-Se bond-center site close to the Se atom, whereas H^0 and H^- occupy equilibrium positions at the interstitial site next to In or Ga.

This work aims to use low energy muons to provide local information on the *p-n* interface of CIGS- and CZTS-based junctions for solar-cell applications. The muon probe will access two different regions in CIGS and CZTS that play an important role in the electric transport properties of the solar cell: (1) the heterojunction interface and the surface of the films; in CIGS, this region is known to be defect rich and exhibit differences in composition and electrical properties when compared to inner regions [25–28]; (2) the absorber space charge region (SCR), negatively charged due to filled acceptor states (the dominant one being the Cu vacancy in Cu-poor CIGS; in CZTS, the main acceptor is the Cu_{Zn} antisite).

The muon probe is sensitive both to charge interactions and to the presence of defects but has not been used before to study *p-n* junctions for solar cells. This work aims to explore the sensitivity of the muon probe in these solar-cell materials. Two films (CZTS and CIGS) were studied by slow muons as well as three *p-n* junctions produced with those films: CdS/CZTS, CdS/CIGS, and ZnSnO/CIGS.

II. EXPERIMENTAL DETAILS

Two different *p-n* junctions, CdS/CIGS and ZnSnO/CIGS, were produced in the Ångström Solar Center, Uppsala University, Sweden, from one single CIGS film, using a test pilot tool for module production. The film had average composition $Cu_{.87}In_{.61}Ga_{.39}Se_2$ and 2-μm thickness. The two *p-n* junction samples had an area $2.5 \times 2.5\,cm^2$, the thickness of the *n*-type layer being 50 nm for CdS and 20 nm for ZnSnO.

In order to study the single CIGS film, the CdS layer was removed from the CdS/CIGS sample by etching with a solution 10% (V/V) of HCl in H_2O, dried with a N_2 blow drier and immediately moved into a N_2 atmosphere to avoid surface oxygenation. It was mounted under continuous N_2 flow in a sample holder and measured in vacuum.

A Cu_2ZnSnS_4 (CZTS) film was produced in Aveiro University, Portugal, with an area $3.0 \times 1.5\,cm^2$ and studied by μSR. An 80-nm CdS layer was then deposited on top of this film by chemical bath deposition and the corresponding CdS/CZTS *p-n* junction was investigated.

The μSR measurements were performed at the μE4 beam line [29] of the Swiss Muon Source, Paul Scherrer Institut, Switzerland, using the low energy muons (LEM) instrument. Positive muons were implanted in the presence of an external magnetic field $B = 10$ mT, in transverse field (TF) geometry and in the temperature range 5–300 K. The muon implantation energy was tuned in the 2- to 25-keV range in order to perform depth-dependent studies in the tens to hundreds of nm range. Figure 2(a) shows the probability per unit length $P(x,E)$ that a muon implanted with energy E stops at a depth x. $P(x,E)$ was obtained by running a Monte Carlo code TRIMSP [30,31] for the CdS/CIGS junction, assuming a 50-nm-thick CdS layer. These simulations also provide information on relative weight of muons stopping on the *n*-type and *p*-type layers, w_n and w_p, respectively, for each muon implantation energy [Fig. 2(b)]. These simulations were performed for all the samples, establishing a correspondence between the muon implantation energy and the average implantation depth for each sample.

The transverse-field μSR time spectra of Cu_2ZnSnS_4 film is similar to what is observed in the bulk sample (Fig. 1). The main component can be described as a Gaussian-damped oscillation at the muon Larmor frequency, corresponding to muons forming a diamagnetic state. The Gaussian relaxation (of the order $\sigma \approx 0.11\,\mu s^{-1}$ in CZTS and $\sigma \approx 0.14\,\mu s^{-1}$ in CIGS) is consistent with nuclear dipolar broadening for muons bound to the anion (S or Se) [32]. A fast relaxing component is also present. The Cu_2ZnSnS_4 film data were therefore fitted with a two-component function of the form:

$$A(t) = A_{\rm dia}\, e^{-\frac{1}{2}\sigma^2 t^2} \cos(\omega t + \phi) + A_{\rm fast} e^{-\lambda t} \cos(\omega t + \phi), \quad (1)$$

where σ and λ are the Gaussian and Lorentzian depolarization rates, respectively. The frequency ω and the phase ϕ were assumed to be the same in both components. In the film spectra there is a difference—usually named as missing fraction—between the maximum asymmetry (obtained from a silver calibration at 200 K) and the total signal amplitude. In LEM experiments, the information at initial times is reduced, since the data below 0.05 μs is related to a superposition of muons decaying in flight and muons already stopped in the sample, and is therefore discarded. Therefore, the fast relaxing component is difficult to separate from the missing fraction due to lack of

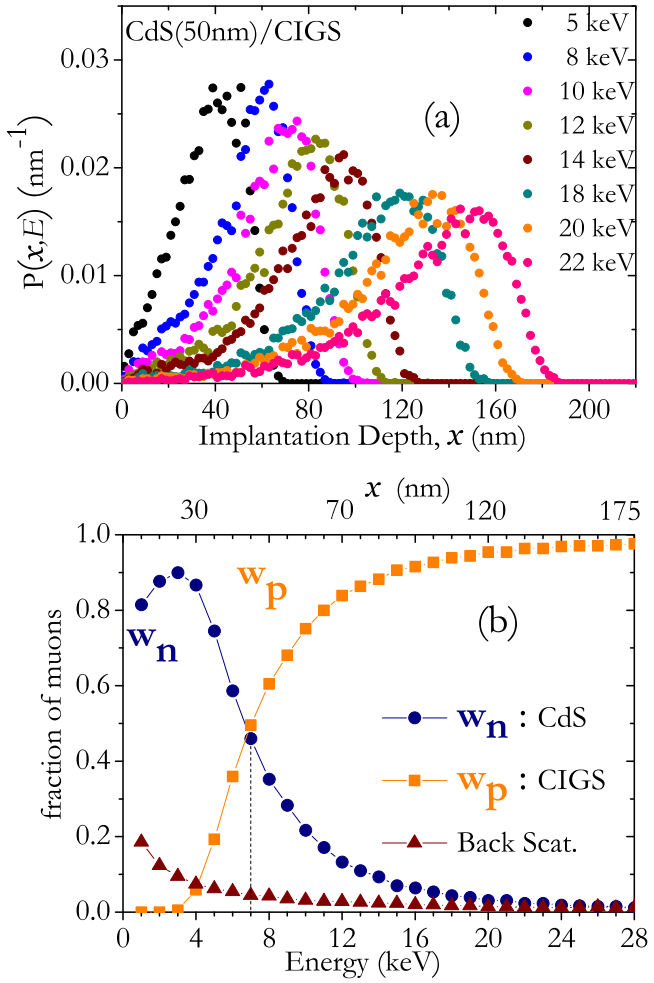

FIG. 2. (a) Muon stopping probability per unit length, $P(x,E)$, for the CdS/CIGS junction, as a function of implantation depth x for different muon implantation energies E. (b) Relative weight of muons stopping on the n-type and p-type layers w_n and w_p, respectively, as a function of the muon implantation energy. The fraction of muons suffering backscattering is also represented.

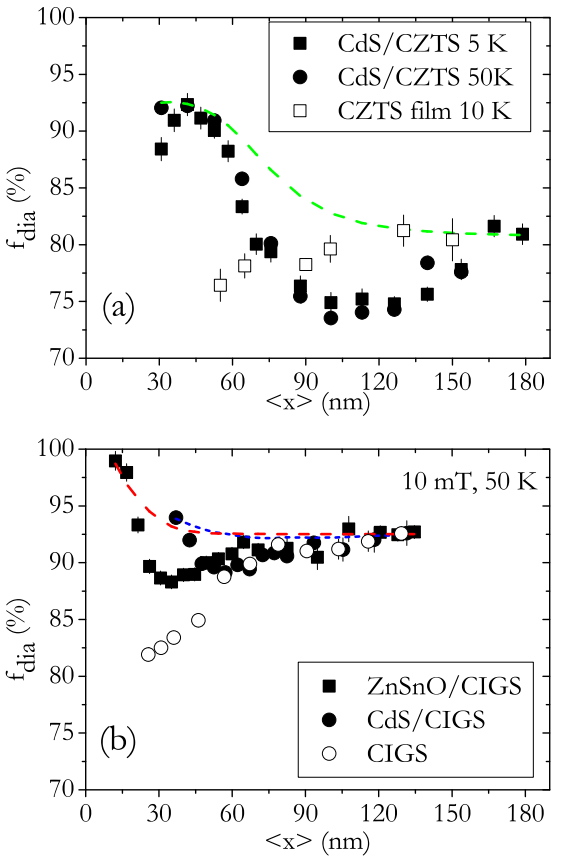

FIG. 3. Diamagnetic fraction as a function of average implantation depth $\langle x \rangle$ for (a) Cu_2ZnSnS_4 (CZTS) film and junction and for (b) Cu(In,Ga)Se_2 (CIGS) film and junctions. The dashed curves are the expected diamagnetic line calculated from the weighted contributions of the n-type and p-type materials (normalized at the end compositions) for CdS/CZTS(green curve, online), ZnSnO/CIGS (red curve, online), and CdS/CIGS (blue curve, online), respectively.

information at initial times and we will not distinguish between the two in the analysis of CZTS data.

No fast relaxing component is observed in the CIGS film, although a fraction of the muon signal is clearly missing. Therefore the following one-component function was used:

$$A(t) = A_{\rm dia}\, e^{-\frac{1}{2}\sigma^2 t^2} \cos(\omega t + \phi). \tag{2}$$

The analysis of the data was performed using the WIMDA software [33]. A silver calibration performed at 200 K, under a transverse field $B = 10$ mT, provided the maximum instrumental asymmetry as a function of the muon implantation energy. The parameter $A_{\rm dia}$ was converted to the corresponding diamagnetic fraction $f_{\rm dia}$, using the silver calibration and a sample size correction, to account for the fraction of muons falling in the sample plate.

III. EXPERIMENTAL RESULTS AND DATA ANALYSIS

A. Implantation depth dependence

Figure 3 shows the diamagnetic fraction $f_{\rm dia}$ as a function of implantation energy for CZTS film and CdS/CZTS junction, as well as for CIGS film, and CdS/CIGS and ZnSnO/CIGS junctions. The value of $f_{\rm dia}$ in the junctions at high muon implantation energies (i.e., at depths where the fraction of muons stopping in the p-type material is $w_p \sim 1$) is similar to the value obtained for the corresponding film at the same energy, and was therefore taken as the characteristic value for that material $f^p_{\rm dia}$. The characteristic value for the n-type material $f^n_{\rm dia}$ was taken from the other end composition. The dashed lines in Fig. 3 are the expected diamagnetic fraction $f^{\rm pred}_{\rm dia}$, calculated as a weighted average of the characteristic values for n-type and p-type materials. The corresponding weights, w_n and w_p, are the values obtained in the Monte Carlo simulations referred to in the experimental section [Fig. 2(b)]:

$$f^{\rm pred}_{\rm dia}(x) = w_n(x)\, f^n_{\rm dia} + w_p(x)\, f^p_{\rm dia}. \tag{3}$$

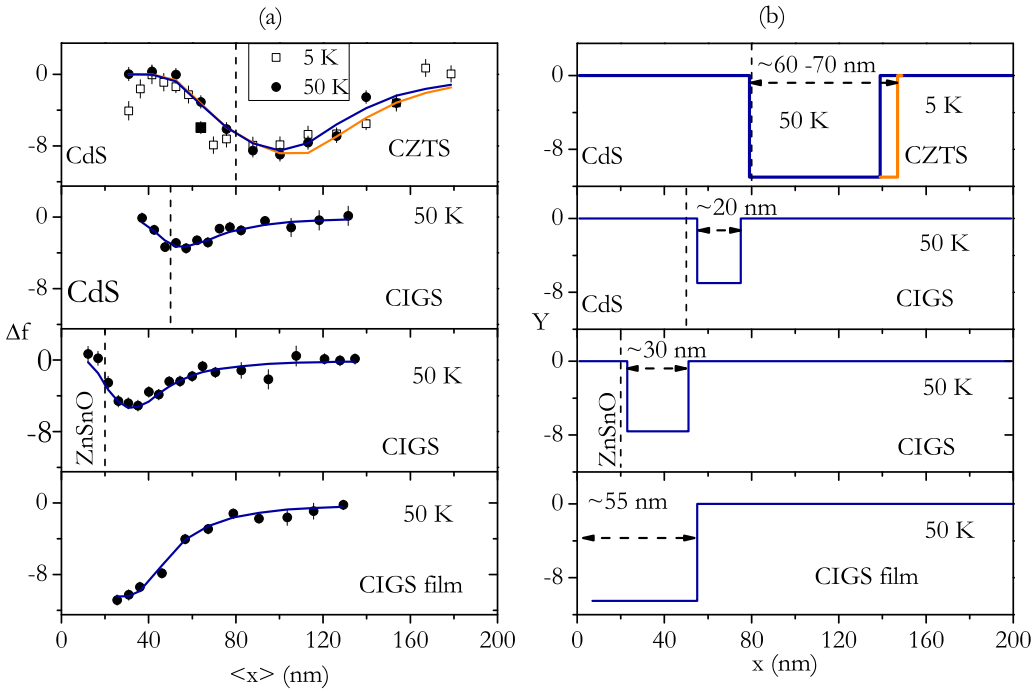

FIG. 4. (a) Variation of the diamagnetic fraction Δf as a function of *average* implantation depth $\langle x \rangle$ for the three junctions and CIGS surface. The dotted vertical lines represent the nominal interface positions. (b) The value of the dip effect Y as a function of depth x, which originates the effect in (a). For simplicity, the Y function is assumed to have a square well shape, with adjustable parameters C, a, and b, representing the depth, beginning, and end of the well, respectively. The full curves in (a) are given by $\Delta f = Y(a,b,C)\ P(a,b,E)$, where $P(a,b,E)$ is the probability that a muon with implantation energy E stops in the range $a < x < b$.

Figure 3 shows that the observed diamagnetic fraction $f_{\rm dia}$ in the *p-n* junctions is clearly lower than predicted, in particular in the region from the junction interface inward into the absorber. For the absorber films alone, a decrease of the diamagnetic fraction is also observed when approaching the film surface, the effect being more pronounced for the CIGS film.

In order to correct for the effect of the composition change in the bilayer samples, the variation of the diamagnetic fraction, $\Delta f = f_{\rm dia} - f_{\rm dia}^{\rm pred}$, is plotted in the left part of Fig. 4 as a function of the average implantation depth. This net effect, Δf, still includes the smoothing due the muon stopping profile [see Fig. 4(a)]. Let's assume, for simplicity, that the physical origin of the drop in the diamagnetic fraction is described by a function $Y(x)$ with a square well shape, as plotted in Fig. 4(b). Thus, $Y = 0$ except in the interval $a < x < b$, where a constant value C is assumed:

$$Y(x) = -C \quad \text{for} \quad a < x < b, \tag{4}$$

where C, a, and b are adjustable parameters, corresponding to the depth, beginning, and end of the square well, respectively. The value for Δf is therefore expected to be zero except in the interval $a < x < b$:

$$\Delta f = -C \quad P(a,b,E) \quad \text{for} \quad a < x < b, \tag{5}$$

where $P(a,b,E)$ is the probability that a muon with implantation energy E stops in the range $a < x < b$. The probabilities $P(a,b,E) = \int_a^b P(x,E)\,dx$ can be easily evaluated by numerical integration of the calculated $P(x,E)$ distributions [see Fig. 2(a)]. The full curves in Fig. 4(a) indicate that this simple assumption leads to a good description of the data, after adjusting the square well parameters (a, b, and C) to the values adopted in Fig. 4(b). It should be noted, however, that a well with a gradual transition at the interface is also consistent with the data. It clearly shows that in the case of the junctions the effect occurs at the *p-n* interface, on the side of the absorber, with a width of the order of 20–30 nm for CIGS and 60–70 nm for CZTS. For the films, it occurs at the surface and has an extension of the order of 55 nm for CIGS. In CZTS film, a decrease of the diamagnetic fraction is also observed with decreasing implantation depth [Fig. 3(a)] but the information is scarce and therefore CZTS film is not included in Fig. 4.

B. Temperature dependence

1. Diamagnetic fraction, interstitial to bound conversion

Figure 5 shows the temperature dependence of the diamagnetic fraction for both CZTS and CIGS. The main feature in both cases is the increase of the diamagnetic fraction above 150 K, more pronounced in CZTS than in CIGS.

As mentioned before, the nondiamagnetic signal is attributed to muonium at an interstitial position whereas the diamagnetic part is mainly due to muons bound to the anion (S or Se). The observed increase of the diamagnetic fraction with increasing temperature is therefore attributed to the thermal-activated conversion of interstitial to bound muonium. The temperature dependence of the diamagnetic fraction was therefore fitted assuming a Boltzmann model:

$$f_{\rm dia} = f_0 + \frac{(100 - f_0)\, N\, e^{-\frac{E_a}{kT}}}{1 + N\, e^{-\frac{E_a}{kT}}}, \tag{6}$$

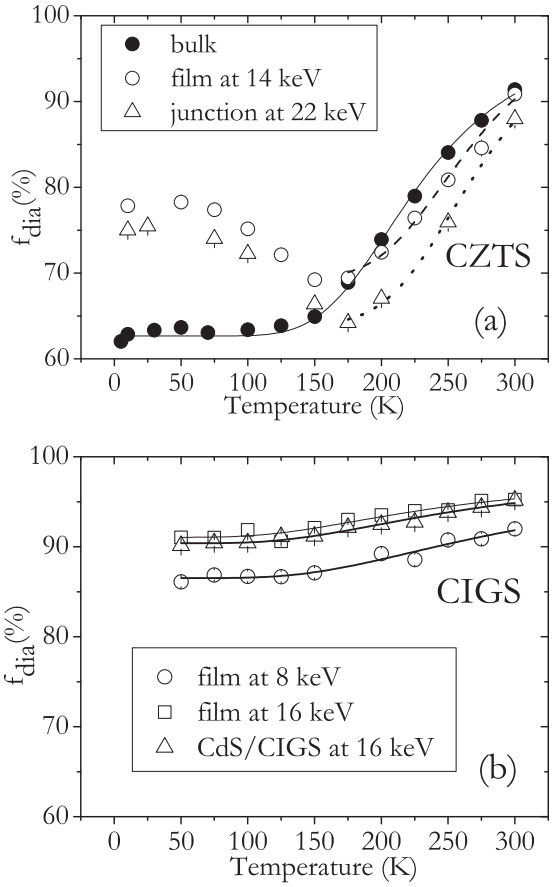

FIG. 5. Temperature dependence of the diamagnetic fraction f_{dia} of CZTS (a) and CIGS (b). The curves describe the increase of the diamagnetic fraction above 150 K as a thermal-activated process, interpreted as a conversion from interstitial to bound muonium. The activation energy for the conversion is clearly larger for the CZTS than for the CIGS material (see Table I).

where f_0 is the initial diamagnetic fraction, before the increase, E_0 is the activation energy for the conversion process, and N is a density of states parameter. The values of N and E_a are strongly correlated. In order to get comparable barrier height values we fixed the statistical factor N in the final fits to $N = 8$ for the CIGS film and $N = 10\,000$ for the CZTS films. These N values are average values from previous fits with free parameters. The activation energies, interpreted as barrier heights for conversion, are presented in Table I.

TABLE I. Activation energies from fitting to Eq. (6).

Sample	E_a(meV)
CZTS bulk	103(5)
CZTS film at 14 keV	158(2)
CZTS junction at 22 keV	162(2)
CIGS film at 8 keV	65(2)
CIGS film at 16 keV	55(3)
CIGS junction at 16 keV	57(2)

The barrier height for the site conversion is clearly larger for CZTS (around 100–160 meV) than for CIGS (in the range 50–70 meV). It is also clear from Fig. 5 that the overall diamagnetic fraction is smaller for CZTS than for CIGS at low temperatures, which is interpreted as a smaller occupancy ratio of the anion-bound site relative to the interstitial one.

In CIGS (Fig. 5), the diamagnetic fraction is constant below 150 K, and the temperature dependence of the CdS/CIGS junction at an implantation energy of 16 keV (corresponding to an implantation depth where 92% of the muons stop in CIGS; see Fig. 2) is consistent with the inward film behavior, given by the film data at an implantation energy of 16 keV. The temperature dependence of the film at 8 keV (i.e., closer to the film surface) is similar, although the overall diamagnetic fraction is lower, as mentioned in the previous section.

In bulk CZTS the diamagnetic fraction is also constant below 150 K, but for CZTS film a distinct temperature dependence behavior is observed. Below 50 K the diamagnetic fraction in the film is significantly larger than the corresponding bulk value (the difference being around 15%) and decreases with increasing temperature between 50 K and 150 K, before the onset of the thermal-activated process. A similar trend is observed in the CdS/CZTS sample at an implantation energy of 22 keV (also corresponding to 92% of the muons stopping in the absorber), although the characteristic film value at inner depths is not yet fully recovered.

2. Depolarization rate, muon diffusion

The temperature dependence of the average depolarization rate of the diamagnetic signal is presented in Fig. 6.

At low temperatures the values are similar for both materials ($\sigma \approx 0.11\ \mu s^{-1}$ in CZTS and $\sigma \approx 0.14\ \mu s^{-1}$ in CIGS) and consistent with nuclear dipolar broadening. The value for CIGS is within experimental uncertainties, the same as measured previously for $CuInSe_2$ [32]. There are slight variations for the low temperature value of the depolarization rate, both for different materials and for the same material (CIGS) at different muon implantation energies, suggesting that there is an additional contribution to the diamagnetic signal. In recent experiments on zirconia [15] a slowly relaxing paramagnetic signal was observed. This signal is attributed to a weakly bound muonium state with an extremely small average hyperfine interaction. It is conceivable that such a state exists also in the present samples and contributes slightly to the broadening of the diamagnetic signal. However, since the nuclear broadening is already large in the present samples, this contribution cannot be separated from the real diamagnetic signal. It may, however, be responsible for the small variations observed in Fig. 6.

The decrease of the depolarization rate with temperature seen in Fig. 6 is interpreted as the onset of diffusion and occurs around the same temperature (∼175 K) in both materials. The temperature at half decay is 240 K and the activation energy is about 60 meV. These values are similar to those found previously for various chalcopyrite samples [34,35].

3. Field shift

All the μSR experiments were performed under an external magnetic field of 10 mT, but the effective field at the muon site

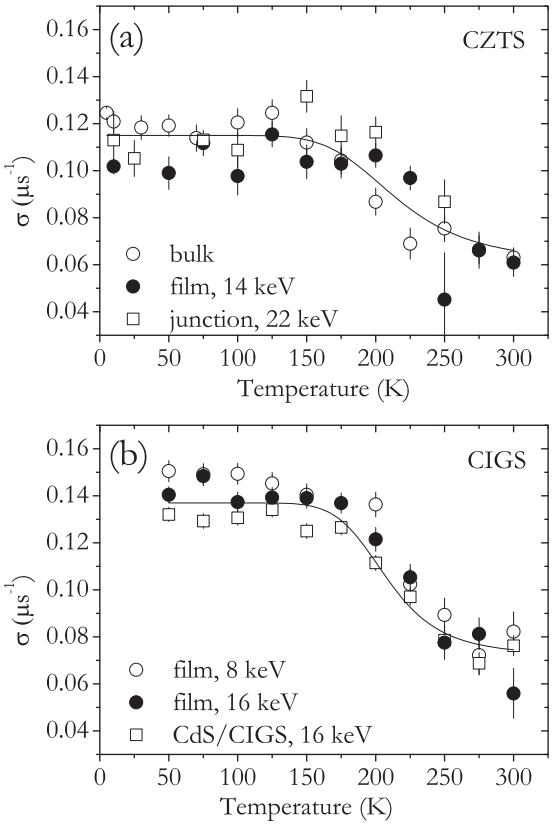

FIG. 6. Temperature dependence of the depolarization rate σ of the diamagnetic signal in CZTS (a) and CIGS (b). A similar decrease of σ above 150 K is observed in all the samples, which is attributed to motional narrowing due to muon diffusion. The lines are a guide to the eye.

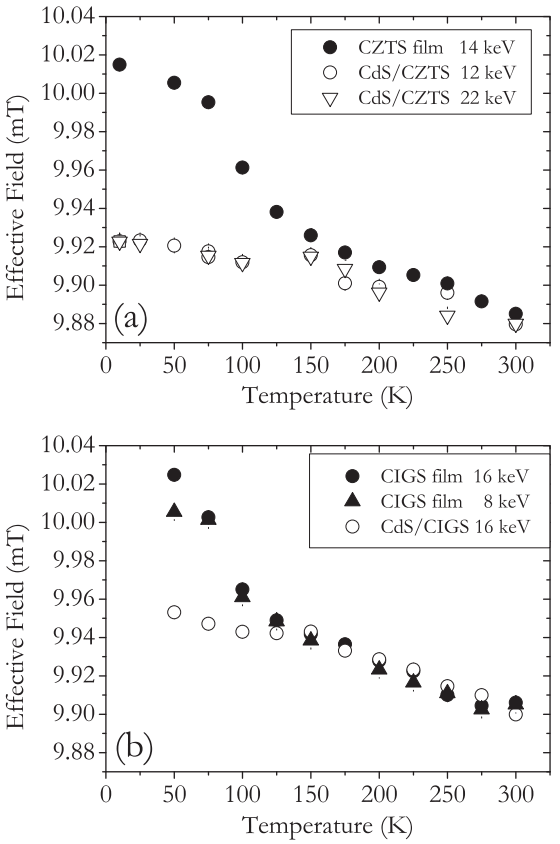

FIG. 7. Effective field at muon site as a function of temperature for CZTS film and CdS/CZTS junction (a) and for CIGS and CdS/CIGS junction (b). All the samples show a similar linear decrease of the effective field above 150 K. An additional upward shift of the effective field is observed below 150 K for the CZTS and CIGS films, when compared with the corresponding materials with a CdS layer on top.

B_{eff} can be determined accurately from the muon precession frequency ω: $B_{\text{eff}} = \frac{\omega}{\gamma_\mu}$, where $\gamma_\mu/2\pi = 1.355 \times 10^8$ Hz/T is the muon gyromagnetic ratio. The effective field at the muon as a function of temperature is plotted in Fig. 7 and is seen to approach the externally applied field at 300 K (as measured through a calibration sample plate; see experimental methods).

A strong increase of the field with decreasing temperature is visible and indicates that a paramagnetic component is contained in the apparently diamagnetic signal.

A seemingly diamagnetic signal with a shifted frequency may be caused by the collapse of the hyperfine lines of paramagnetic muonium at its center position, due to an electron spin dynamics [36] or to muon jumps between nearly equivalent sites, as observed in TiO_2 [16]. In the Paschen-Back region, the average muonium frequency coincides with the diamagnetic line, but an upward shift is expected if the external field approaches the Zeeman region. In the present case, the external magnetic field is $B = 10$ mT and therefore an upward shift of the magnitude observed in Fig. 7 requires a hyperfine interaction in the order of one to several MHz, a value similar to what has been observed in the oxygen-bound position in TiO_2 [16]. A signature of a muonium state with a hyperfine interaction of the order of 2–3 MHz was observed previously in $CuInSe_2$, at low temperatures and high magnetic fields [37]. Similar effects to those observed in Fig. 7 were also reported in completely different systems, namely at the surface of n-doped commercial Ge and GaAs wafers [38], in SnO_2 [39], and even in semimetals such as Sb [6]. In those cases, the effect was also attributed to muonium with a hyperfine interaction of a few MHz, suffering a very rapid charge exchange [6].

Interestingly, the upward shift observed below 150 K for the CZTS and CIGS films, disappears when the CdS layer is added (see Fig. 7). This indicates that the contribution of weakly bound muonium to the signal is reduced. The effect is not fully understood yet. A possible explanation is that the built-in electric field at the junction reduces the binding energy of the electron and decreases the formation of this weakly bound muonium state, as suggested elsewhere [40].

IV. DISCUSSION

A. Interpretation of muonium fractions

The main result in this work is the observation of a dip in the diamagnetic fraction at the p-n interfaces and at the film's surface. It is therefore important to discuss the interpretation of the diamagnetic signal and its interplay with the fast and missing signals.

The diamagnetic fraction is attributed to muons in an anion-bound position, either in a positive or neutral charge

state $Mu^{+/0}_{bound}$. The slowly relaxing paramagnetic signal, if it exists in these samples (see discussion above), is included in the diamagnetic fraction since we cannot separate these two components experimentally.

The fraction corresponding to the fast and missing signals is related to the neutral at an interstitial position Mu^{0}_{atom}, suffering a strong loss of polarization.

The Mu^{0}_{atom} related fraction may include two different contributions: a quasiprompt component, where interstitial muonium is formed directly after muon implantation and a delayed formation of muonium via the quasidiamagnetic, transition state which converts to atomlike muonium [40].

We did not observe the typical μSR frequencies expected for a prompt atomlike muonium in our measurement. Thus, if this component is present, the dephasing during lattice relaxation is too strong and destroys the polarization. Therefore, this contribution is seen in the μSR spectrum as a missing signal. It is important to notice that muons formed promptly at an interstitial position, in the unrelaxed lattice, are in an excited, nonrelaxed configuration. If we designate this excited state as Mu^{0*}_{atom}, the complete polarization loss, due to lattice relaxation and consequent changes of hyperfine interaction, is described by $Mu^{0*}_{atom} \rightarrow Mu^{0}_{atom}$. Any subsequent conversion of Mu^{0}_{atom} to a diamagneticlike species will not affect the observed diamagnetic fraction since the polarization is already fully lost.

The second contribution for the Mu^{0}_{atom} fraction involves an intermediate quasidiamagnetic state which exists for some time as a precursor of atomlike muonium. The intermediate state corresponds to the fast relaxing signal mentioned above [40]. It may not be seen in the μSR spectrum if the lifetime of the intermediate state is too short for the μSR time window. In this latter case, this delayed component is contained in the missing fraction.

The observed changes in the missing/diamagnetic fractions with muon implantation energy require that a fraction of the promptly formed Mu^0 suffers either a charge change (converting to Mu^+ or Mu^-) or a site change (from the interstitial to the anion-bound position). The charge conversion to Mu^-, however, is likely to be followed by a hole capture in a p-type material. A possible exception is the case where the muon stops in a hole-depleted region. In the depleted region, however, the built-in electric field repels the electrons generated by the muon track towards the n-type material, inhibiting Mu^- formation. Thus, the negative charge state Mu^- is not likely to play a significant role in the experimental findings and will be not considered.

Two main mechanisms are proposed to explain the observed changes in the diamagnetic fraction.

(i) Change of the fraction Mu^0/Mu^+ of the two relevant muonium states formed in the charge exchange cycle; this change would be due to hole capture either during the rest of the muon path before stopping or immediately after stopping. A long precursor lifetime can be excluded since we see no phase shift of the diamagnetic signal.

(ii) Change of the branching between interstitial and bound muonium (or muon) during the conversion of the initial to the final configuration.

In both mechanisms (i) and (ii), the muon at the anion-bound configuration $Mu^{0/+}_{bound}$ may exist in two charge states, both seen as a diamagneticlike signal (as discussed in III B 2 and in III B 3):

$$Mu^{0}_{bound} \rightleftharpoons Mu^{+}_{bound} + e^{-}.$$

This electron loss or capture does not affect the nominal (or so-called) diamagnetic fraction, but can be a source of the observed small changes in the average depolarization rate and of average muon frequency (Figs. 6 and 7).

The two different mechanisms (i) and (ii) give rise to two different models as discussed below.

B. Models

1. Energy band diagram

Before addressing the proposed models it is worthwhile to consider the schematic energy band diagram of the heterojunction CdS/CIGS presented in Fig. 8.

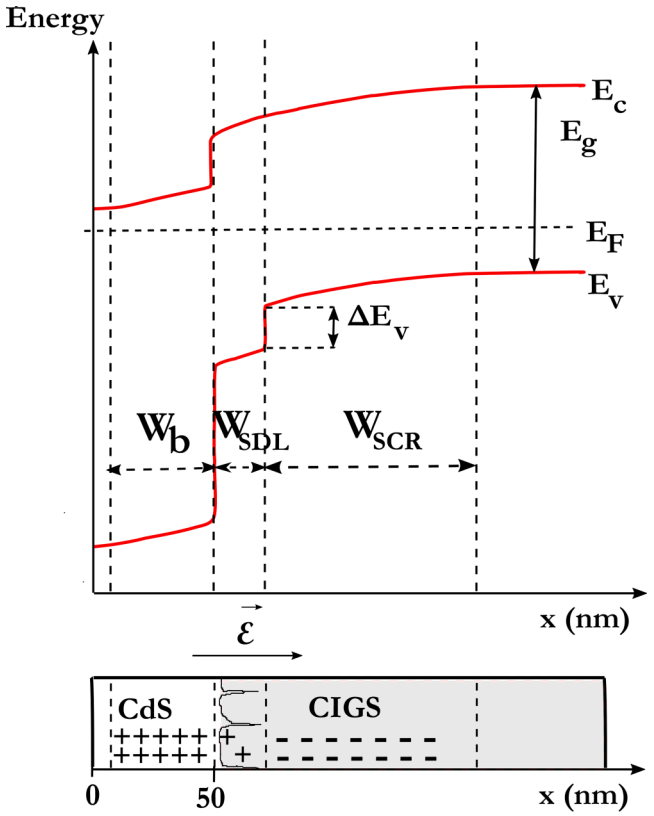

FIG. 8. Schematic energy band diagram of the CdS/CIGS heterostructure (adapted from Turcu and Rau [27]). E_C, E_V, E_F, and E_g denote the conduction band edge, the valence band edge, the Fermi energy, and the band gap of the absorber at inner depths, respectively. SDL stands for surface defect layer and SCR for space charge region. ΔE_V is the valence band offset introduced by the SDL [27]. W_b is the width of the depleted buffer layer. W_{SDL} and W_{SCR} are the widths of the corresponding regions, both in the absorber. The interface between the SDL and CdS is not a plane surface perpendicular to the muon beam, therefore the width of the SDL seen by the muon is enlarged, especially if the surface shape is very irregular (as in CZTS) and if it extends to grain boundaries (as in CIGS film [41] and possibly in CZTS).

As expected, there is a depleted, space charge region (SCR) in the p-type absorber, where the acceptors are negatively charged. The CIGS surface exhibits a different composition and electric properties compared to the bulk of the absorber and different models have been proposed to describe its defect-rich surface layer. We will concentrate here on the model of the *surface defect layer* (SDL) [26–28,42] since it is both well accepted and fully consistent with the μSR findings. The absorber SDL has a Cu-deficient composition, when compared to the inner bulk, and exists in as-grown films and in complete heterojunction devices [26–28]. The SDL is described as a defect-rich, disordered surface layer with a net positive surface charge due to dangling bonds, associated with Se vacancies acting as donors [41–44]. This positive charge causes a type inversion at the CIGS surface and as a consequence, the p-n transition in the heterostructure is shifted from the CdS/CIGS interface to the transition between the SDL and SCR regions [26,27,45]. When the buffer layer is CdS, additional composition changes are observed in the SDL due to the diffusion of Cd ions into CIGS [46,47]. Inside the space charge region (SCR) grain boundaries may also have a positively charged surface [48], which play an important role in the solar-cell device performance [46,49,50]. This problem is particularly important in CZTS samples which possess a small grain structure when compared with state-of-the-art CIGS.

2. Space charge region (SCR) model

In this model, the muon is sensitive to the net charge within the absorber space charge region.

The ratio between the missing signal and the diamagnetic fraction depends, within this model, on the fate of muonium at the interstitial site, namely if its stays neutral or captures a hole:

$$\mathrm{Mu}^{0*}_{\mathrm{atom}} \rightarrow \mathrm{Mu}^{0}_{\mathrm{atom}} \tag{7}$$

$$\text{or} \quad \mathrm{Mu}^{0*}_{\mathrm{atom}} + \mathrm{h}^{+} \rightarrow \mathrm{Mu}^{+}_{\mathrm{atom}}. \tag{8}$$

The dip in the diamagnetic fraction is observed in the absorber SCR, characterized by the absence of free carriers and a local net charge density. Process 8 is inhibited in the absorber SCR, due to the depletion of holes. Thus, within the SCR model, for a given material, at a given temperature, the diamagnetic fraction f_{dia} depends on the concentration of holes. If, for simplicity, we assume a linear dependence of the hole concentration, f_{dia} will be given by

$$f_{\mathrm{dia}} = f^{0}_{\mathrm{dia}} + b\, c_{\mathrm{hole}}, \tag{9}$$

where f^{0}_{dia} is the diamagnetic muon fraction in the absence of holes, c_{hole} is the concentration of holes, and b is a proportionality constant. In the SCR region, $f_{\mathrm{dia}} = f^{0}_{\mathrm{dia}}$, and the diamagnetic fraction is reduced.

Within the SCR model, the dip in the diamagnetic fraction of Fig. 4 would be due to the depletion of holes and the width of the dip would correspond to an effective SCR width in the absorber. The effect is expected to be constant within the dip, consistent with observation.

Capacitance measurements were performed at room temperature for our CdS/CIGS sample and yield 120 nm for the total SCR width [51], a value relatively small when compared with values in the range 200–300 nm, obtained for similar samples [52–55]. Those values were obtained at room temperature and include both the n-type and p-type depleted regions whereas the μSR results are sensitive only to the p-type region and were obtained at 50 K. If a fully depleted CdS layer is assumed, 50-nm wide, then from measured 120 nm for the total SCR width one can estimate a lower limit of around 70 nm for the absorber SCR width in CIGS, at room temperature. The observed dip widths of 20–30 nm for CdS/CIGS and ZnSnO/CIGS (Fig. 4) are clearly smaller than expected for the absorber SCR width at room temperature. Furthermore, it is known that interface defects and deep traps in CIGS increase the measured capacitance at room temperature [25,42]. Temperature-dependent C-V measurements indicate that the SCR width obtained at room temperature is underestimated by a factor of around two [42,56]. If the SCR width at 50 K is about twice the measured value of 120 nm, then the muon beam does not reach the end of the SCR, even at the highest implantation energies. The 20- to 30-nm dip widths observed for CdS/CIGS and ZnSnO/CIGS in Fig. 4 seem therefore unrealistic values for the space charge region in CIGS.

Additionally, a dip of the diamagnetic fraction is also observed in the single CIGS film, near its surface, which would be interpreted as the formation of a depletion layer due to surface-type inversion. This surface band bending is destroyed upon air exposure of the film due to the passivation of the surface donors by oxygen [46]. In our case, air exposure was mitigated (see experimental details) and a high density of positive charge is likely to be present at the film surface and at grain boundaries [48]. The charges at grain boundaries extend the SCR deeper into the film, as suggested by Rau and Schock [41]. Assuming a typical density of positive surface states in CIGS [42,46] of the order of 10^{12} cm^{-2} and a net acceptor density [57] of the order of 6×10^{16} cm^{-3}, the width of the space charge region in CIGS film can be estimated to be around 160 nm, using a charge neutrality condition. Values of the order of 300 nm are mentioned in the literature [42].

The dip of the diamagnetic fraction for the CIGS film observed in Fig. 4 is 55-nm wide. Therefore, in spite of being larger than the corresponding dip in the CdS/CIGS junction, it still seems too small to be a measure of the space charge region width in these materials.

3. Surface defect layer (SDL) model

In this model the muon is being sensitive to defect-rich, disordered regions such as the SDL.

The ratio between the missing signal and the diamagnetic fraction is interpreted within this model as the outcome of a competition between the two following processes:

$$\mathrm{Mu}^{0*}_{\mathrm{atom}} \rightarrow \mathrm{Mu}^{0}_{\mathrm{atom}} \tag{10}$$

$$\text{or} \quad \mathrm{Mu}^{0*}_{\mathrm{atom}} \rightarrow \mathrm{Mu}^{0/+}_{\mathrm{bound}}. \tag{11}$$

The site change from the interstitial to the anion-bound configuration is likely to be hindered by the presence of a defect-rich, disordered region such as the SDL, existing both at the junction interface and at the surface of single layers. In other words, the conversion of interstitial to bound muonium evolves

via an energy barrier, and the barrier height may be higher in defect-rich or poorly organized structures, as suggested by calculations performed for Y stabilized zirconia [58]. In analogy to Eq. (9), we write for the measured diamagnetic muon fraction $f_{\rm dia}$,

$$f_{\rm dia} = f^0_{\rm dia} - g(c_{\rm defects}), \tag{12}$$

where $f^0_{\rm dia}$ is the expected diamagnetic fraction in the absence of defects, and $g(c_{\rm defects})$ is a monotonic function of the defect concentration. Note that we may have different kinds of defects and the sensitivity may not necessarily be proportional to the concentration of defects.

In this model, the decrease of the diamagnetic fraction near the *p-n* interface and near the surface, observed in Fig. 4, is attributed to the presence of defects/structural disorder in these regions.

In Fig. 4, the width and depth of the dip is much more significant for the bare CIGS absorber than for the corresponding heterostructures. As discussed in the literature [41], in the bare absorber the positively charged defects extend from the film surface to the grain boundaries, penetrating at inner depths [see Ref. [41], Figs. 9(a)–9(c)]. Air exposure passivates both surfaces. After a chemical bath deposition of CdS, defects at grain boundary surfaces remain passivated whereas the type inversion is recovered near the CdS interface due to the high ammonia concentration of the chemical bath deposition [59]. This is compatible with the effect observed in Fig. 4 which is both wider and deeper in the bare film. The ZnSnO/CIGS was produced from the same CIGS film of the CdS/CIGS sample. Therefore, the ZnSnO also seems to play a protective role on the absorber surface, although slightly less effective than CdS, since the dip observed in Fig. 4 is deeper for ZnSnO/CIGS when compared to CdS/CIGS.

The dip in the diamagnetic fraction in CdS/CZTS is also much deeper and longer than in CdS/CIGS. This is attributed in this model to its known inferior electronic quality, with a larger density of interface defects, distributed in a much more irregular surface, seen by the muon as an effective width. This is also consistent with the results in Table I where the barrier height for a thermal-activated conversion of interstitial to bound muonium was found to be larger in CZTS than in CIGS material. The power conversion efficiencies are also considerably lower in CdS/CZTS-based solar cell compared with CdS/CIGS-based ones, as expected for a less perfect material.

In summary, within this model, the width of the defected areas, as seen by the muon probe, varies between 20 nm and 70 nm depending on the material and material's combination. An irregular surface and a contribution from grain boundaries are expected to increase the effective width of the SDL, as seen by the muon. This enhancement should be particularly evident in the bare CIGS surface and in CdS/CZTS, as observed.

V. CONCLUSIONS

Our measurements show a dip of the diamagnetic μSR fraction in the absorber near the buffer/absorber interface and near the surface of the bare film. We examined whether the dip stems from processes occurring in the SCR or is likely to have its origin in the SDL.

In the SCR model, the smaller diamagnetic fraction of the dip could be due to the fact that the incoming muonium can lose an electron to holes in the bulk but not in the depletion region. In this model the width of the dip would correspond to the width of the SCR. However, there is no correspondence of the dip width with the SCR width, even if one takes into account large uncertainties. Thus we conclude that the dip in the present experiment cannot be attributed to the SCR. It is important to note that this conclusion is based on the relative change of the observed muonium fractions in this family of materials and does not exclude a general sensitivity of the muon probe to electrical charges and built-in electric fields, namely in systems where the μSR spectrum contains a clear signature of a neutral muonium state.

In the SDL model, the conversion of incoming muonium to diamagnetic muon proceeds via a potential barrier and this barrier is higher in distorted defect-rich lattice regions than in the bulk. In this model, the width of the dip corresponds to the width of the SDL region. Here we have agreement between experiment and expectation: The smallest distorted region (20 nm) is found for the CdS/CIGS sample whereas the CdS/CZTS and the unprotected CIGS surface show larger disturbances (50–70 nm).

We conclude that μSR provides a measure of the surface defect layer width both in the heterostructures and in the films. Our experiment indicates that the buffer layer, especially CdS, has a protective and healing effect on the absorber, in agreement with previous suggestions [41]. Good interfaces are crucial for the performance of solar cells and this work opens a new path in the study of the influence of defects in the interface properties of complex multinary semiconductors, using the μSR technique.

ACKNOWLEDGMENTS

We are grateful to the PSI machine and beamline groups whose outstanding efforts have made these experiments possible. This work was supported with funds from FEDER (Programa Operacional Factores de Competitividade COMPETE) and from FCT–Fundação para a Ciência e Tecnologia under Projects No. PTDC/FIS/102722/2008 and No. UID/FIS/04564/2016.

[1] R. Kamada, T. Yagioka, S. Adachi, A. Handa, K. F. Tai, T. Kato, and H. Sugimoto, in *2016 IEEE 43rd Photovoltaic Specialists Conference (PVSC)* (IEEE, Piscataway, 2016), pp. 1287–1291.

[2] W. Wang, M. T. Winkler, O. Gunawan, T. Gokmen, T. K. Todorov, Y. Zhu, and D. B. Mitzi, Adv. Energy Mater. **4**, 1301465 (2014).

[3] J. Lindahl, J. T. Wätjen, A. Hultqvist, T. Ericson, M. Edoff, and T. Törndahl, Prog. Photovolt: Res. Appl. **21**, 1588 (2013).

[4] S. F. J. Cox, R. L. Lichti, J. S. Lord, E. A. Davis, R. C. Vilão, J. M. Gil, T. D. Veal, and Y. G. Celebi, Phys. Scr. **88**, 068503 (2013).

[5] R. C. Vilão, J. M. Gil, A. Weidinger, H. V. Alberto, J. P. Duarte, N. A. de Campos, R. L. Lichti, K. H. Chow, and S. F. J. Cox, Nucl. Instrum. Methods Phys. Res., Sect. A **580**, 438 (2007).

[6] S. F. J. Cox, Rep. Prog. Phys. **72**, 116501 (2009).

[7] B. D. Patterson, Rev. Mod. Phys. **60**, 69 (1988).

[8] T. Prokscha, E. Morenzoni, D. G. Eshchenko, N. Garifianov, H. Glückler, R. Khasanov, H. Luetkens, and A. Suter, Phys. Rev. Lett. **98**, 227401 (2007).

[9] T. Prokscha, E. Morenzoni, D. Eshchenko, H. Luetkens, G. Nieuwenhuys, and A. Suter, Physica B **404**, 866 (2009).

[10] T. Prokscha, K. H. Chow, E. Stilp, A. Suter, H. Luetkens, E. Morenzoni, G. J. Nieuwenhuys, Z. Salman, and R. Scheuermann, Sci. Rep. **3**, 2569 (2013).

[11] H. V. Alberto, R. C. Vilão, J. P. Duarte, J. M. Gil, A. Weidinger, J. S. Lord, and S. F. J. Cox, Phys. Rev. B **86**, 035203 (2012).

[12] H. V. Alberto, A. Weidinger, R. C. Vilão, J. P. Duarte, J. M. Gil, J. S. Lord, and S. F. J. Cox, Phys. Rev. B **81**, 245205 (2010).

[13] H. V. Alberto, R. C. Vilão, J. M. Gil, J. Piroto Duarte, R. B. L. Vieira, A. Weidinger, J. P. Leitão, A. F. da Cunha, M. Sousa, J. P. Teixeira *et al.*, Int. J. Mod. Phys.: Conf. Ser. **551**, 012045 (2014).

[14] T. Prokscha, H. Luetkens, E. Morenzoni, G. J. Nieuwenhuys, A. Suter, M. Döbeli, M. Horisberger, and E. Pomjakushina, Phys. Rev. B **90**, 235303 (2014).

[15] R. B. L. Vieira, R. C. Vilão, A. G. Marinopoulos, P. M. Gordo, J. A. Paixão, H. V. Alberto, J. M. Gil, A. Weidinger, R. L. Lichti, B. Baker *et al.*, Phys. Rev. B **94**, 115207 (2016).

[16] R. C. Vilão, R. B. L. Vieira, H. V. Alberto, J. M. Gil, A. Weidinger, R. L. Lichti, B. B. Baker, P. W. Mengyan, and J. S. Lord, Phys. Rev. B **92**, 081202 (2015).

[17] P. W. Peacock and J. Robertson, Appl. Phys. Lett. **83**, 2025 (2003).

[18] A. G. Marinopoulos, R. C. Vilão, R. B. L. Vieira, H. V. Alberto, J. M. Gil, M. V. Yakushev, R. Scheuermann, and T. Goko, Philos. Mag. **97**, 2108 (2017).

[19] E. L. da Silva, A. G. Marinopoulos, R. B. L. Vieira, R. C. Vilão, H. V. Alberto, J. M. Gil, R. L. Lichti, P. W. Mengyan, and B. B. Baker, Phys. Rev. B **94**, 014104 (2016).

[20] R. C. Vilão, A. G. Marinopoulos, R. B. L. Vieira, A. Weidinger, H. V. Alberto, J. P. Duarte, J. M. Gil, J. S. Lord, and S. F. J. Cox, Phys. Rev. B **84**, 045201 (2011).

[21] E. Morenzoni, H. Glückler, T. Prokscha, H. Weber, E. Forgan, T. Jackson, H. Luetkens, C. Niedermayer, M. Pleines, M. Birke *et al.*, Physica B **289-290**, 653 (2000).

[22] T. Prokscha, K. Chow, H. Luetkens, E. Morenzoni, G. Nieuwenhuys, Z. Salman, R. Scheuermann, A. Suter, and H. Weber, Physics Procedia **30**, 219 (2011).

[23] C. Kilic and A. Zunger, Appl. Phys. Lett. **83**, 2007 (2003).

[24] C. Kilic and A. Zunger, Phys. Rev. B **68**, 075201 (2003).

[25] U. Rau, D. Abou-Ras, and T. Kirchartz, *Advanced Characterization Techniques for Thin Film Solar Cells* (Wiley, New York, 2011).

[26] T. Dullweber, G. Hanna, U. Rau, and H. W. Schock, Sol. Energy Mater. Sol. Cells **67**, 145 (2001).

[27] M. Turcu and U. Rau, J. Phys. Chem. Solids **64**, 1591 (2003).

[28] M. Turcu and U. Rau, *Recombination Mechanisms in Cu(In,Ga)(Se,S)$_2$ Solar Cells* (Springer, Berlin/Heidelberg, 2006).

[29] T. Prokscha, E. Morenzoni, K. Deiters, F. Foroughi, D. George, R. Kobler, A. Suter, and V. Vrankovic, Nucl. Instrum. Methods Phys. Res., Sect. A **595**, 317 (2008).

[30] E. Morenzoni, H. Glückler, T. Prokscha, R. Khasanov, H. Luetkens, M. Birke, E. Forgan, C. Niedermayer, and M. Pleines, Nucl. Instrum. Methods Phys. Res., Sect. B **192**, 254 (2002).

[31] W. Eckstein, *Computer Simulations of Ion-Solid Interactions* (Springer, Berlin/Heidelberg, New York, 1991).

[32] J. M. Gil, P. J. Mendes, L. P. Ferreira, H. V. Alberto, R. C. Vilão, N. Ayres de Campos, A. Weidinger, Y. Tomm, C. Niedermayer, M. V. Yakushev *et al.*, Phys. Rev. B **59**, 1912 (1999).

[33] F. Pratt, Physica B **289-290**, 710 (2000).

[34] R. C. Vilão, Master's thesis, Faculdade de Ciências e Tecnologia–Universidade de Coimbra, 2002, http://hdl.handle.net/10316/2558.

[35] R. C. Vilão, J. M. Gil, H. V. Alberto, J. Duarte, N. A. de Campos, A. Weidinger, M. Yakushev, and S. F. J. Cox, Physica B **326**, 181 (2003).

[36] J. M. Gil, J. P. Duarte, R. C. Vilão, H. V. Alberto, N. A. de Campos, and S. F. J. Cox, Physica B **404**, 834 (2009).

[37] R. C. Vilão, H. V. Alberto, J. M. Gil, J. P. P. Duarte, N. A. de Campos, A. Weidinger, and M. Yakushev, Physica B **340-342**, 965 (2003).

[38] T. Prokscha *et al.* (unpublished).

[39] A. Rabis, T. Prokscha, E. Fabbri, Z. Salman, T. Schmidt, and A. Suter [JPS Conf. Proc. (to be published)].

[40] R. C. Vilão, R. B. L. Vieira, H. V. Alberto, J. M. Gil, and A. Weidinger, Phys. Rev. B **96**, 195205 (2017).

[41] U. Rau and H. W. Schock, Appl. Phys. A **69**, 131 (1999).

[42] R. Herberholz, U. Rau, H. W. Schock, T. Haalboom, T. Gödecke, F. Ernst, C. Beilharz, K. W. Benz, and D. Cahen, Eur. Phys. J. Appl. Phys. **6**, 131 (1999).

[43] S. Schleussner, U. Zimmermann, T. Wätjen, K. Leifer, and M. Edoff, Sol. Energy Mater. Sol. Cells **95**, 721 (2011).

[44] A. Rockett, D. Liao, J. Heath, J. Cohen, Y. Strzhemechny, L. Brillson, K. Ramanathan, and W. Shafarman, Thin Solid Films **431-432**, 301 (2003).

[45] R. Klenk, Thin Solid Films **387**, 135 (2001).

[46] U. Rau, D. Braunger, R. Herberholz, H. W. Schock, J.-F. Guillemoles, L. Kronik, and D. Cahen, J. Appl. Phys. **86**, 497 (1999).

[47] P. M. P. Salomé, R. Ribeiro-Andrade, J. P. Teixeira, J. Keller, T. Törndahl, N. Nicoara, M. Edoff, J. C. González, J. P. Leitão, and S. Sadewasser, IEEE J. Photovolt. **7**, 858 (2017).

[48] C.-S. Jiang, M. A. Contreras, I. Repins, H. R. Moutinho, Y. Yan, M. J. Romero, L. M. Mansfield, R. Noufi, and M. M. Al-Jassim, Appl. Phys. Lett. **101**, 033903 (2012).

[49] Y. Yan, C.-S. Jiang, R. Noufi, S.-H. Wei, H. R. Moutinho, and M. M. Al-Jassim, Phys. Rev. Lett. **99**, 235504 (2007).

[50] C.-S. Jiang, R. Noufi, J. A. AbuShama, K. Ramanathan, H. R. Moutinho, J. Pankow, and M. M. Al-Jassim, Appl. Phys. Lett. **84**, 3477 (2004).

[51] P. M. P. Salomé, J. P. Teixeira, J. Keller, T. Törndahl, S. Sadewasser, and J. P. Leitão, IEEE J. Photovolt. **7**, 670 (2017).

[52] P. M. P. Salomé, A. Hultqvist, V. Fjällström, M. Edoff, B. Aitken, K. Vaidyanathan, K. Zhang, K. Fuller, and C. K. Williams, IEEE J. Photovolt. **3**, 852 (2013).

[53] P. M. P. Salomé, V. Fjällström, P. Szaniawski, J. P. Leitão, A. Hultqvist, P. A. Fernandes, J. P. Teixeira, B. P. Falcão, U. Zimmermann, A. F. da Cunha *et al.*, Prog. Photovolt: Res. Appl. **23**, 470 (2015).

[54] V. Fjällström, P. Szaniawski, B. Vermang, P. M. P. Salomé, F. Rostvall, U. Zimmermann, and M. Edoff, IEEE J. Photovolt. **5**, 664 (2015).

[55] A. Hultqvist, P. M. P. Salomé, V. Fjällström, M. Edoff, B. Aitken, K. Zhang, Y. Shi, K. Fuller, and C. K. Williams, J. Appl. Phys. **114**, 094501 (2013).

[56] G. F. Brown, Ph.D. thesis, Materials Science & Engineering, UC Berkeley, 2011.

[57] P. M. P. Salomé, J. Keller, T. Törndahl, J. P. Teixeira, N. Nicoara, R.-R. Andrade, D. G. Stroppa, J. C. González, M. Edoff, J. P. Leitão *et al.*, Sol. Energy Mater. Sol. Cells **159**, 272 (2017).

[58] R. B. L. Vieira, R. C. Vilão, P. M. Gordo, A. G. Marinopoulos, H. V. Alberto, J. P. Duarte, J. M. Gil, A. Weidinger, and J. S. Lord, Int. J. Mod. Phys.: Conf. Ser. **551**, 012050 (2014).

[59] L. Kronik, U. Rau, J.-F. Guillemoles, D. Braunger, H.-W. Schock, and D. Cahen, Thin Solid Films **361-362**, 353 (2000).